RSC Advances

PAPER

View Article Online
View Journal | View Issue

Cite this: *RSC Adv.*, 2023, **13**, 3877

Flexible doctor blade-coated abiotic cathodes for implantable glucose/oxygen biofuel cells†

Myriam Ghodhbane, *[ab] Gauthier Menassol,[bc] Davide Beneventi,[a] Didier Chaussy,[a] Lionel Dubois,[c] Abdelkader Zebda[b] and Mohamed Naceur Belgacem [a]

Implantable devices powered by batteries have been used for sixty years. In recent devices, lithium-based batteries are the most widely used power source. However, lithium batteries have many disadvantages in terms of safety, reliability, and longevity and require regular monitoring and substitution. Implantable glucose biofuel cells (BFCs) are increasingly seen as a potential future technology for replacing lithium-based batteries because they do not require surgical replacement after 8–10 years and have a theoretically unlimited lifetime thanks to the continued recovery of glucose and oxygen present in the human body. This paper shows the fabrication of flexible implantable abiotic cathodes, based on a nitrogen/iron-doped graphene catalyst, for glucose/oxygen biofuel cell application. An ink, based on nitrogen-iron doped graphene as the abiotic catalyst and chitosan as a binder, was prepared and coated on a flexible teflonated gas diffusion layer using doctor blade coating. The characterization of the biocathode shows an open potential circuit corresponding to the potential of the abiotic catalyst and a high oxygen reduction current density of up to 66 μA cm^{-2} under physiological conditions. Those cathodes remain stable for up to two years with a current density loss of only 25%. The flexible abiotic electrode cytotoxicity was evaluated by cell culture experiments showing living cells' high tolerance on the biocathode surface. This work demonstrates that this abiotic catalyst can be a promising alternative for the development of implantable glucose BFCs due to its stability and its cytocompatibility.

Received 6th June 2022
Accepted 21st November 2022

DOI: 10.1039/d2ra03471a

rsc.li/rsc-advances

1. Introduction

In recent decades, medicine has seen a huge development in the field of implantable medical devices (IMDs) treating several health defects affecting patients ranging from birth defects to organ failure. Recent studies indicate that 6% of the industrialized countries' populations have used an IMD.[1] Some IMDs, called active IMDs, such as pacemakers and neurostimulators must rely on permanent and sufficient electrical power. The first electrical power source developed to supply IMDs was lithium-ion based-batteries. The latter ones have been used for sixty years,[2] since the first successful pacemaker implantation in 1960.[3] To date, they remain the first choice for supplying power. Each day, new IMDs are appearing, either to replace older devices or to enable new treatments. Technical progress has made it possible to fabricate artificial organs.[4] Still, one key obstacle for realizing such devices is powering them after implantation. Unfortunately, the lithium-ion-based battery's size and lifetime fail to reach these new IMD generation conditions. Thus, instead of periodically removing them and replacing their batteries, researchers would prefer that those machines somehow harvest energy directly from their hosts. For this reason, implantable glucose biofuel cells (BFCs) are increasingly seen as a potential future technology for replacing lithium batteries.[5] These fuel cells can generate electricity from the anodic oxidation of glucose and the cathodic reduction of dissolved oxygen which are already present in the human body.[6] Unlike lithium-ion batteries, this type of battery has a theoretically unlimited lifetime thanks to the continuous glucose and oxygen recovery from the human body. Scientists have already shown that GBFCs implanted in rats can successfully generate electricity from the glucose and oxygen present in rodents' bodies.[7]

As a function of the catalyst type used at the bioelectrodes, GBFCs can be classified into two types: (i) enzymatic biofuel cells, where enzymatic catalysts are used, and (ii) abiotic biofuel cells relying on abiotic catalysts. Actually, abiotic biofuel cells are gradually attracting great interest. For applications requiring continuous and prolonged operation time,[8] the use of abiotic catalysts in implantable glucose biofuel cells is preferable over enzymes.[8] This is mainly because of their potential superior stability since they do not suffer from progressive denaturation over time.

[a]*Univ. Grenoble Alpes, CNRS, Grenoble INP, Institute of Engineering Univ. Grenoble Alpes, LGP2, Grenoble 38000, France*

[b]*Univ. Grenoble Alpes/CNRS/INSERM/TIMC-IMAG UMR 5525, Grenoble, 38000, France*

[c]*Univ. Grenoble Alpes, CEA, CNRS, IRIG-SyMMES, Grenoble 38000, France*

† Electronic supplementary information (ESI) available. See DOI: https://doi.org/10.1039/d2ra03471a

Even though the first implanted biofuel cell in the 1960s was abiotic, only a few studies have been devoted to this topic. The most used abiotic catalysts for both the anode and the cathode are noble metals-based catalysts. However, platinum high cost and rarity limit its use.[9] Besides, the platinum-based catalyst gets empoisoned by the chloride ions present in the physiological fluids. In recent works, several efforts were devoted to replacing this kind of catalyst with free noble metal catalysts. In this context, catalysts based on carbides and metal nitrides are promising materials to replace nobel metals used for oxygen reduction reaction (ORR) such as iron and/or cobalt precursors supported on carbon support doped with nitrogen. The overall catalyst performance of the product is attributed to the simultaneous and interactive presence of these components. It has been demonstrated by Dodelet *et al.*[9] and largely confirmed by experiments, that nitrogen is a necessary component of the catalyst active site. Therefore, a nitrogen-containing precursor must often be added to the synthesis reaction during catalyst preparation. The most commonly used nitrogen precursors are NH_3,[10] acetonitrile,[11] pyrrole[12] and nitrogen-containing polymers.[13] Faubert *et al.*[14] have demonstrated that the use of NH_3 for the pyrolysis step not only induced the incorporation of nitrogen atoms in the carbon support but also modified the carbon microstructure by creating micropores. However, a clear understanding of the change in coordination or the evolution of the structure during heat treatment is absent. The nature of the obtained active sites is still under discussion.[15] The main advantage of the abiotic catalysts is their capacity to operate under physiological condition and their long-term stability.

In this context, graphene materials seem to be very promising compared to the commonly used carbon materials (*i.e.* graphite and amorphous carbon), graphene has greater electrical and thermal conductivity, better mechanical resistance, and a large surface area.[16] Thereafter, the use of graphene in the glucose biofuel cell field is attracting ever-increasing attention. Graphene is used for both the anodic and cathodic materials, showing excellent performances on either glucose oxidation or oxygen reduction.[17] Most of the graphene-based abiotic catalysts were tested in basic media, and only a few investigations in neutral media were done[18,19]. Newly, Su *et al.*[20] fabricated a non-enzymatic glucose fuel cell using graphene sheets grafted with platinum and palladium for glucose oxidation and nitrogen-doped graphene oxide for oxygen reduction. These catalysts showed a power density of 15 $\mu W\ cm^{-2}$ in a 4 mM glucose solution under oxygen flow and at 25 °C.

Recently, 3D electrodes for glucose/oxygen biofuel cells have been developed by Zebda *et al.*[7] through a compression method. Thanks to these electrodes, it is currently possible to use a larger active material in a smaller surface area. However, using a compression manufacturing method, compact electrodes suffering from low electrolyte diffusion within the electrode are obtained. In fact, the electrode thickness and density hinder glucose and oxygen diffusion thus affecting the biofuel cell electrochemical performances. Besides, this electrode's type is relatively bulky and fragile. This rigidity could cause problems especially for implantable BFCs that may be damaged during the movement.

On another note, flexible BFCs have been manufactured for a long time. Different substrates were employed such as carbon fibers[21,22] carbon nanotube films,[23] gas diffusion layers[26] as well as cellulose substrates coated with conductive ink.[24] Different coating techniques were also used to fabricate this type of BFCs, ranging from traditional coating methods like brushing,[25] casting to more sophisticated automated processes like screen printing,[24,26–28] and ultrasonic spraying.[29] Even though these flexible electrodes are more adapted for implantable applications, it is limited by the quantity of active material deposited per surface, hence by a low electrochemical performance per surface unit. Using the doctor blade coating method will allow us to obtain a larger quantity of material compared to the other used methods such as ultrasonic spraying,[29] screen printing[24,26–28] and spin coating,[30] *etc.* while maintaining the electrolyte diffusion at the electroactive majority surface level.

The doctor blade is a well-established coating method that allows the formation of uniform flat films on large surfaces with a well-defined thickness. This method presents two major advantages when it comes to the fabrication of abiotic electrodes: the first one is the fact that the losses in terms of ink are minimal around 5% of the initial quantity, which makes it possible to obtain functional films with a small ink amount, this is a very important advantage especially when it comes to a small-scale catalyst manufacturing. Moreover, this method ensures a thicker film formation compared to the other used methods which are necessary to achieve a good catalytic activity, especially when using no noble metal abiotic catalysts. Furthermore, this method is also inexpensive and easy to operate. The method's operational principle consists of placing a cutting blade at a fixed distance from the substrate surface (generally between 10–500 μm). The coating solution is then placed in front of the slide which will then be moved linearly over the substrate leaving a thin wet film as illustrated in Fig. 1.

The doctor blading method may be carried out manually or automatically where the shear field is relatively small, and the linear velocities are generally between 1–100 $mm\ s^{-1}$. Generally, the final wet film thickness is ideally half the width of the gap but may vary due to the substrate surface energy, the coating solution surface tension, and the ink viscosity.[31] In general, the

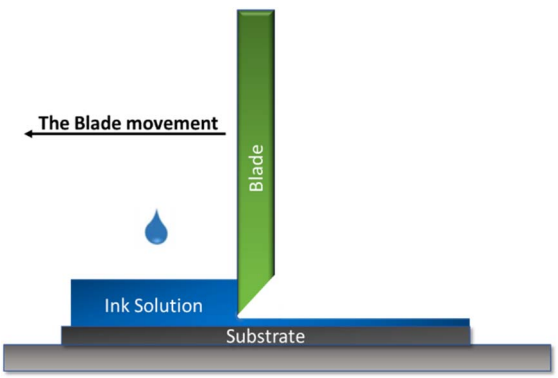

Fig. 1 Schematic illustration of the doctor blade printing working principle.

wet film thicknesses obtained by this method are ranging from 20 to several hundred microns.[32] The doctor blade coating technique was seldomly used in the field of glucose/oxygen biofuel cell manufacturing. Concerning the enzymatic glucose biofuel cell, few works were realized dealing with enzymatic glucose biofuel cells fabricated using doctor blade[33,34]. Regarding the abiotic glucose/oxygen biofuel cell, this coating method has been more used in comparison with the enzymatic ones. S. Kerzenmacher *et al.*[8] have well explored this field. They started by making an abiotic glucose/oxygen biofuel cell prototype made of an activated carbon-based catalyst for the oxygen reduction and two types of binders, *i.e.*, Polyvinyl Alcohol (PVA) and Polyacid Acrylate (PAA). The anode consists of a mixture of activated carbon and a Pt–Bi platinum alloy. Both cathodes were made using the doctor blade method. A power up to 20 μW cm^{-2} was obtained for 7 days.[13,29] More detailed studies on the manufacturing process of biofuel cells and a detailed analysis of their long-term performance in a neutral buffer containing physiological quantities of glucose and oxygen were performed by the same group resulting in a power density in the range of (3.3 ± 0.2) μW cm^{-2} during 10 days reaching a value of (1.0 ± 0.05) μW cm^{-2} after 224 days.[35]

Since biofuel cells are dedicated to medical applications, good electrochemical performance is not enough. Biocompatibility is also an important criterion controlling whether the implant is accepted or not by the organism. In this context, cytocompatibility tests are considered us screening tests performed for the purpose to evaluate the reaction of living cells towards the implant and compare it with their normal behaviors. From these tests, it is possible to determine cell viability and the cell's ability to grow in the presence of the implant in question. It is often recommended by ethics committees to carry out these tests before implanting the object in order to ensure its non-cytotoxicity. A material is cytotoxic if its presence causes a cell necrosis phenomenon characterized by a rapid cell death followed by cell lysis. During this phenomenon, the cells will generally undergo a swelling followed by a loss of the integrity of their membrane and metabolic arrest. The final step of this phenomenon is characterized by the release of the cell's content in the environment causing then an inflammatory reaction. Cell culture testing in the presence of the material in question gives us a quick idea about the material toxicity. However, this test is specific to a certain cell type. Indeed, it is necessary to choose the cell's type in such a way that it is possible according to the obtained results to get pieces of information about the potential interactions between the body and the material once implanted. Several studies carried out have proven the cytotoxicity of chitosan[36,37] and reduced graphene oxide.[38,39] The cells chosen within the framework of this work in order to carry out our preliminary cytocompatibility tests are embryonic fibroblast-like cells derived from the mice, the 3T3-L1. This type of cell is frequently used in the literature and it is among the cells authorized in the standard ISO.[40–42]

In the present work, we investigate the use of iron/nitrogen-doped graphene as ORR catalyst for abiotic flexible biocathode dedicated for implantable GBFCs. Firstly, a chitosan-doped graphene-based ink formulation was optimized. This ink was then used for the cathode layer deposition on carbonated porous paper. Physical and morphological characterizations were achieved to characterize the morphological features of deposited biocathodes. Electrochemical performances show that these biocathodes are able to catalyze the oxygen reduction rection under physiological conditions with a lifetime stability of more than two years. The cathode's cytocompatibility was then validated using 3T3 mice cells opening then the possibility for *in vivo* tests.

2. Experimental part

2.1. Products

All chemicals and reagents used in this study were analytical grade and used as received without further purification. Graphene nanoplates aggregates (sub-micron particles, surface area 750 m^2 g^{-1}) referred as (Gr) in this work, purchased from Stream, research-grade commercial carbon nanotubes CNTs (Thin MWCNTs 95% C purity NC3100™) from Nanocyl Belgium, chitosan low molecular weight (Cs), acetic acid, Genipin, $FeCl_3 \cdot 6H_2O$, Tween 80 and Nafion 117 5% from Sigma Aldrich. Gas diffusion layer (GDL) Fi2C6 was purchased from PaxiTech France.

2.2. Nitrogen-iron doped graphene synthesis

The synthesis method of the iron-nitrogen doped graphene, consists firstly of dispersing 16 g of graphene nanoplatelets aggregates in 500 mL of water. Then 0.32 g (2 wt%) of $FeCl_3 \cdot 6H_2O$ was added. After being sonicated for two hours in order to have a homogenous dispersion, the mixture was freeze-dried. The resulting powder was annealed for two hours at 800 °C with a temperature increase of 20 °C min^{-1} in an ammonia/argon atmosphere (40/60, 10 mL min^{-1}). The resultant catalyst was soaked over night in 0.5 M sulfuric acid, and then washed several times with pure water up to a pH of 7.

2.3. Cathodes fabrication

2.3.1. Graphene/chitosan-based ink. 150 μL of acetic acid were added to 20 mL of deionized water and heated to 60 °C. Once the temperature reached 60 °C, 0.2 g of chitosan was added to the heated solution. The chitosan was completely dissolved after 2 h of stirring. Then, 150 μL of the genipin solution (6 mg mL^{-1}) was added and let it react under stirring for 1 h. Finally, 2 g of commercial graphene nanoplates aggregates were added to the mixture. The mixture was put in a bath sonicator for 1 h. Finally, the graphene nanoplates aggregates/chitosan-based ink was stirred over the night at 700 rpm.

2.3.2. Cathode preparation. In order to increase the ink wettability with the GDL, a primer adhesion layer was firstly added to the gas diffusion layer. Twenty five layers of carbon nanotubes (CNTs)-based ink were sprayed over the gas diffusion layer according to the process used previously by Ben Tahar *et al.*[29] Briefly, an ink of 0.5% of carbon nanotube was prepared: in 20 mL of deionized water 250 mg of carbon nanotube and 300 mg of tween 80 were sonicated at 20 W for 1 h 30 min using a probe sonicator: a Branson digital sonifier 250 with

Table 1 Summary table of the different ink compositions (percentage of dry solids, coated ink weight per surface, and the number of passes using the hand coater)

Sample	D. Gr : Gr : Cs	Percentage on dry solids	Coated ink weight per surface (g cm^{-2})	Pass number using hand coater
Sample 1	27 : 10 : 1	28%	0.014	1
Sample 2	18 : 10 : 1	22.8%	0.016	2
Sample 3	14 : 10 : 1	20%	0.018	3
Sample 4	11 : 10 : 1	18.2%	0.02	4

a titanium-based alloy probe of 1 cm of diameter. The prepared ink was spray coated on the gas diffusion layer surface using a Prism 500 ultrasonic spray coater supplied by USI, Ultrasonic Systems, Inc. at a basis weight of 0.65 mg m^{-2} (which corresponded to the deposition of 25 layers).

For the ink formulation optimization, a series of experiments were realized as follow: different quantities of the graphene/chitosan-based ink were mixed with 100 mg of the catalyst (2% iron–nitrogen doped graphene referred here as D. Gr) in order to obtain different (doped graphene : graphene nanoplates : chitosan) ratios (D. Gr : Gr : Cs) of 27 : 10 : 1, 18 : 10 : 1, 14 : 10 : 1 and 11 : 10 : 1 (see Table 1). The catalyst mass percentage in the dry ink ranged between 18.2 wt% and 28 wt%. The mass catalyst coated per the GDL surface varied from 0.014 g cm^{-2} to 0.02 g cm^{-2} as shown in Table 1. The cathodic ink was coated on a CNTs sprayed commercial gas diffusion layer using a hand doctor blade coater with a 250 μm slot. Different passes were realized according to the ink composition as described in Table 1. To realize the electrode's electric contact, an electric contact wire was glued to the not-printed face of the prepared electrodes using a carbon paste.

3. Cathode's characterizations

3.1. Physical characterization. X-ray powder diffraction data of a fine powder of the different ink compound fine powder were collected at room temperature using the Xpert Pro MPD (multipurpose diffractometer). The sample was contained in a thin-walled borosilicate glass capillary with a diameter of 1.0 mm. The wavelength used for data collection is a K alpha copper (1.54 Å) using a θ/θ system, and the data were collected in the 2θ range 10–60°.

Printed surfaces were characterized using several techniques to check the coated surface homogeneity, to measure the printed layer thickness, and also to verify the good adhesion between the CNTs modified substrate and the coated layer. The flexible electrodes surface topography and the surface roughness were measured using a surface profilometer, *i.e.* optical microscope with focal length variation (Alicona Infinite Focus). A magnification of (10×) was used. The surface roughness was determined according to the ISO 4288, 5 images of 1 cm were recorded for each sample. Five roughness measurements were made for each image. Surface and cross-sectional views of the printed GDL were recorded through Scanning electron microscopy (SEM) imaging. An environmental scanning electron microscope (ESEM, Quanta 200 FEI, Hillsboro, Oregon, USA) was used at a high voltage equal to 12.2 kV and a working distance equal to 10.2 mm. The surface of the printed GDL was observed using a Zeiss ultra 55 FESEM microscope. A micrometer was used to estimate the coated layer thickness. 10 Measurements were performed for each sample to calculate the mean thickness value. N_2 physisorption tests were performed to measure the specific area of each sample where 70 mg of each sample were dried at 105 °C for 12 hours then analyzed, with a Novae (Quatachrome) analyzer in a pressure range between 0.1 to 0.3 bar. The electrodes' electrical conductivity was measured by a four-tip cylindrical probe system combined with an impedance analyzer type RM3000 (Jandel Universal Probe System with RM3-AR unit test) at 25 °C. The voltage was measured by varying the current between 10 mA and 90 mA, then the $f(U) = i$ curves were plotted. The slope of this curve indicates the square resistance. The contact angle measurements were carried out by depositing different ink droplets at the substrate surface (the commercial GDL and the CNTs-modified GDL) and recording the contact angles formed using an OCA dataphysics system equipped with a CCD camera. During the first 60 seconds, the contact angle and the drop volume acquisition were realized after deposition. Four images per second were taken. All measurements were performed 10 times for each sample.

3.2. Electrochemical characterizations. The electrochemical characterizations were performed using three electrodes electrochemical cell-associated to a Biologic Potentiostat SP150. The printed biocathode was used as a working electrode, a platinum electrode was used as a counter electrode, and a saturated calomel electrode (SCE) as a reference electrode. The abiotic biocathodes were tested in physiological media (100 mL) of a solution containing phosphate buffer (0.01 mol L^{-1}), NaCl (0.14 mol L^{-1}), KCl (0.0027 mol L^{-1}), pH = 7.4 at ambient temperature (20 ± 3 °C). Cyclic voltammetry measurements were carried out using a rotating electrode disc (0.001 cm^2) between 1 V and −1 V at a scan rate of 10 mV s^{-1} and a rotating disc speed of 500 rpm. Due to the chitosan-based ink weak adhesion on glassy carbon surface, we used Nafion solution to prepare the doped graphene-nafion based ink. This one was prepared by the addition of 2 mg of Nafion 117 5% and isopropanol (0.22/0.78 N) solution. 100 μL of the prepared ink was deposited into the surface of glassy carbon (0.07 cm^2) and left to dry under air for 1 hour. Cyclovoltammetry of the D. Gr under air nitrogen and oxygen, in a phosphate-buffered saline solution (PBS) pH = 7.4 at a scan rate of 10 mV s^{-1} and a rotating disk electrode (RDE) speed of 500 rpm was then performed.

The cathode's chronoamperometric response (CA) was recorded at 0.1 V *vs.* a saturated calomel electrode (SCE) for 24 h. The abiotic cathode characterizations were performed using a conventional three-electrode cell with a saturated calomel electrode as a reference electrode and a platinum auxiliary electrode. The flexible prepared abiotic cathodes play the role of the working electrodes. A frequency between 10 kHz and 50 kHz was applied at the open circuit voltage (OCV) potential. The cathode stability was evaluated after different aging periods (1 month, 2 months, 1 year, and 2 years). Five cathodes were stored in a PBS solution at room temperature. After each period, their current density was evaluated by recording their chronoamperometric response at 0.1 V *vs.* SCE for 24 h. Finally, an average of the delivered current density of five samples was obtained for each period.

4. Results and discussion

4.1. Optimization of the cathodic ink formulation

4.1.1. Ink characterization. The X-ray diffraction studies were done for four samples: pure low molecular weight (LMW) chitosan (Cs), graphene nanoplates aggregates (Gr), nitrogen/iron 2% doped graphene nanoplates aggregates (D. Gr), and the final prepared ink. Fig. 2 shows that pure chitosan exhibits 2 broad peaks at $2\theta = 10°$ and $2\theta = 20°$: the broad peak at $2\theta = 10.5°$ was associated with the hydrated crystals corresponding to the remained α-chitin chains in raw chitosan,[43] whereas the peak at $2\theta = 20.08°$ with the partial crystalline chitosan structure[44] indicating corresponding indices (020) and (110). The commercial graphene nanoplates, the nitrogen-iron doped graphene, and the final ink samples exhibit three peaks one at $2\theta = 26.5°$, one at $2\theta = 43.5°$ and the third one at $2\theta = 54.7°$. The measurement results of these three samples are comparable and show only the carbon contributions. The two peaks obtained at $2\theta = 26.5°$ and $2\theta = 43.5°$ indicate the typical graphitic C(002) and C(100) turbostratic carbon structure.[45] The 2 peaks obtained at $2\theta = 43.5°$ and $2\theta = 54.7°$ are large peaks characteristic of the amorphous phases. Sometimes, doping graphene may induce a little negative shift of the graphitic C(002) plane explained by an increase in the interlayer-distance due to the incorporation of N and/or Fe in the carbon framework as demonstrated for the Fe–N–C catalyst synthesized by Ketpang *et al.*[19] and He *et al.*,[45] However, this wasn't the case for us may be cause of the low doping percentage. As mentioned before, the final prepared ink has the same peaks as the graphene nanoplates and doped graphene, however, the diffraction line C(002) plane peak is wider since it is a mixture between the doped graphene, the graphene nanoplates, and chitosan.

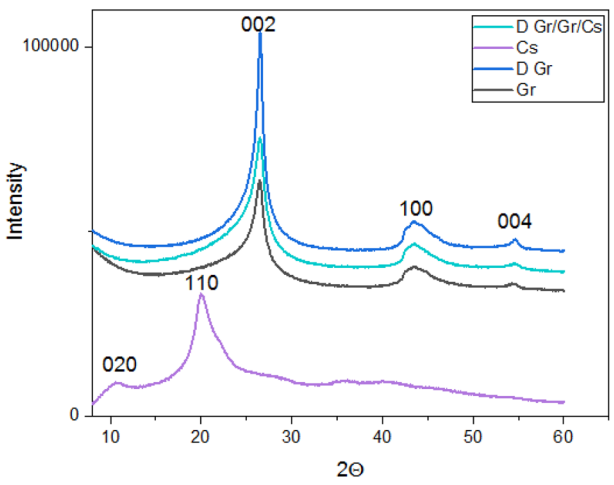

Fig. 2 XRD patterns of the prepared ink (D. Gr/Gr/Cs), chitosan, doped graphene (D. Gr) and Graphene (Gr).

The interplanar distance was calculated according to the Bragg theory (eqn (1)):

$$n\lambda = 2d\sin\theta \quad (1)$$

where $n =$ is an integer determined by the given order. $\lambda =$ is the wavelength of X-rays, and moving electrons, protons, and neutrons. $d =$ is the spacing between the planes in the atomic lattice. $\theta =$ is the angle between the incident ray and the scattering planes.

The results are summarized in Table 2:

4.1.2. Primary adhesion layer. An adhesion layer was firstly deposed on the gas diffusion layer by spraying 25 layers of a CNTs-based ink according to the process used previously by Ben Taher *et al.*[29] Fig. 3 shows the surface and cross-section view of the CNTs sprayed gas diffusion layer.

As shown in Fig. 4, we demonstrated through the contact angle measurement, the improvement of ink wettability when it comes to the CNTs modified gas diffusion layer. The contact angle changes from a value of $\theta = 137° \pm 6°$ to $\theta = 37° \pm 8°$ by adding an adhesion layer based on carbon nanotubes and Tween 80. In fact, the use of the tween 80 as a dispersant induces the increase of the GDL surface hydrophilicity once the ink is sprayed on the surface. Which explains the wettability amelioration for the CNTs-modified gas diffusion layer as demonstrated previously by A. Laaroussi *et al.*[46]

4.1.3. Coated layer characterization. As described in Table 3, four different samples with different (doped graphene :

Table 2 Summary of the calculated interplanar distances for each sample

	Peak 1	Peak 2	Peak 3
Chitosan LMW (Cs)	$2\theta = 10°$, $d = 8.83$ Å	$2\theta = 20.0°$, $d = 4.43$ Å	—
Graphene nanoplates (Gr)	$2\theta = 26.5°$, $d = 3.36$ Å	$2\theta = 43.5°$, $d = 1.12$ Å	$2\theta = 54.7°$, $d = 0.94$ Å
Doped graphene (D. Gr)	$2\theta = 26.5°$, $d = 3.36$ Å	$2\theta = 43.5°$, $d = 1.12$ Å	$2\theta = 54.7°$, $d = 0.94$ Å
The prepared ink	$2\theta = 26.5°$, $d = 3.36$ Å	$2\theta = 43.5°$, $d = 1.12$ Å	$2\theta = 54.7°$, $d = 0.94$ Å

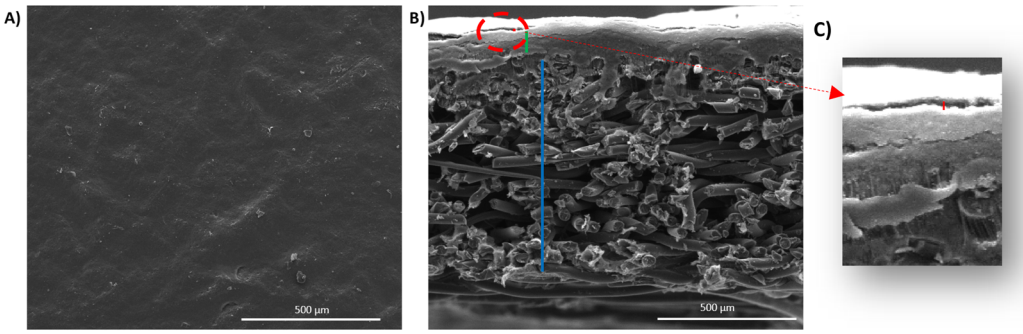

Fig. 3 (A) Surface views of the CNTs-sprayed ink on the gas diffusion layer top (GDL) top. (B) Cross-section images of the CNTs-sprayed gas diffusion layer (GDL), where the red line for the sprayed layer, the green line for the GDL nano-porous layer (NPL), and the blue line for the GDL micro-porous layer (MPL). (C) Zoom from the image (B) showing the sprayed nanotubes layer (designed with a red line).

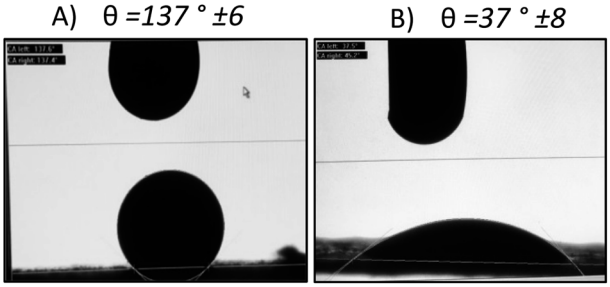

Fig. 4 (A) The contact angle of the GDL and the graphene/chitosan/doped graphene-based ink: 137° ± 6°. (B) The contact angle of the CNTs sprayed GDL and the graphene/chitosan/doped graphene-based ink: 37° ± 0.8°.

graphene nanoplates : chitosan) ratios (D. Gr : Gr : CS) (see Table 3), were prepared in order to identify the best formulation in terms of adhesion between the coated layer and the CNTs modified substrate and electrochemical activity. For the different formulations, the ratio between the graphene nanoplates and chitosan was kept constant, and the doped graphene ratio changed.

The coated layer's thicknesses varied from 92 µm to 210 µm (see Table 3) and samples square resistance between 1.8 and 0.77 (mm Ω square^{-1}). The 3D topography images and the SEM images were done to check the coated surface's homogeneity (see Fig. 5 and 6). A measure of the sample's surface area was done using the N_2 physisorption method. The obtained results are summarized in Table 3.

• For sample 1, the scanning electron microscopy and the 3D topography images demonstrate a coated layer heterogeneity. A bad adhesion with the CNTs modified substrate was also noticed especially when doing the electrochemical tests. This is due principally to the low binder mass fraction compared to the total graphene quantity.

• For sample 2, the coated layer is homogenous, and good adhesion between this one and the substrate was obtained. No micro crackles were observed on the coated surface as shown by 3D topography images (Fig. 5). Besides, through the scanning electron microscopic (SEM) images shown in Fig. 6, a high microporosity was observed which is also validated by the highest surface area value compared to the other samples as shown in Table 3 (68.86 m^2 g^{-1}). For this sample, the quantity of the coated ink was enough to cover the substrate and to keep a high porosity owing to no layer stacking as in samples 3 and 4.

• For sample 3, some microscopic crackles were observed on the coated surface (see Fig. 5 and 6).

• However, for sample 4, the coated layer thickness was important (263 ± 8 µm), leading to numerous micro crackle formations. Thus, the coated layer flakes off. This fact induces a weak adhesion with the CNTs-modified substrate, and a lower conductivity value compared to the other samples (705 Ω cm^{-1}).

In samples 3 and 4, the surface porosity was lower than in sample 2, as shown in the SEM images (Fig. 6). In fact, this is due principally to the higher deposited material quantity. Indeed, the stacking of layers induces a lower microscopic porosity, as supported by surface area values in Table 3 (11.33 m^2 g^{-1} for sample 3, 28.50 m^2 g^{-1} for sample 4, and 68.86 m^2 g^{-1} for sample 2).

Table 3 The prepared electrodes composition and characteristics

Sample number	D. Gr : Gr : Cs	Thickness (µm)	Conductivity (Ω cm^{-1})	Surface area (m^2.g^{-1})
GDL	—	224 ± 1	1539	10.37
GDL + NCT	—	226 ± 1	1526	10.72
Sample 1	27 : 10 : 1	92 ± 5	1084	18.75
Sample 2	18 : 10 : 1	100 ± 4	1058	68.86
Sample 3	14 : 10 : 1	203 ± 8	1138	11.33
Sample 4	11 : 10 : 1	263 ± 8	705	28.5

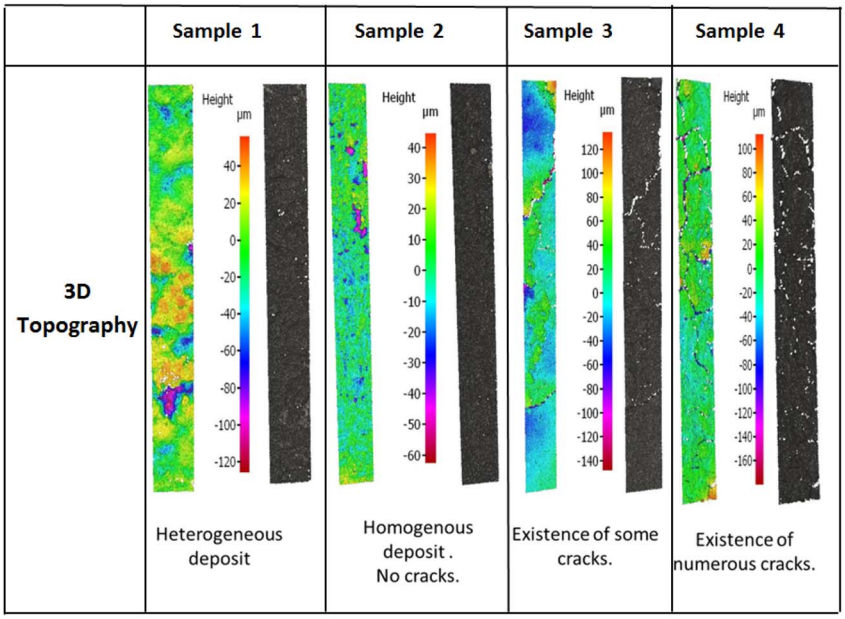

Fig. 5 3D topography images using Alicona for the four prepared samples.

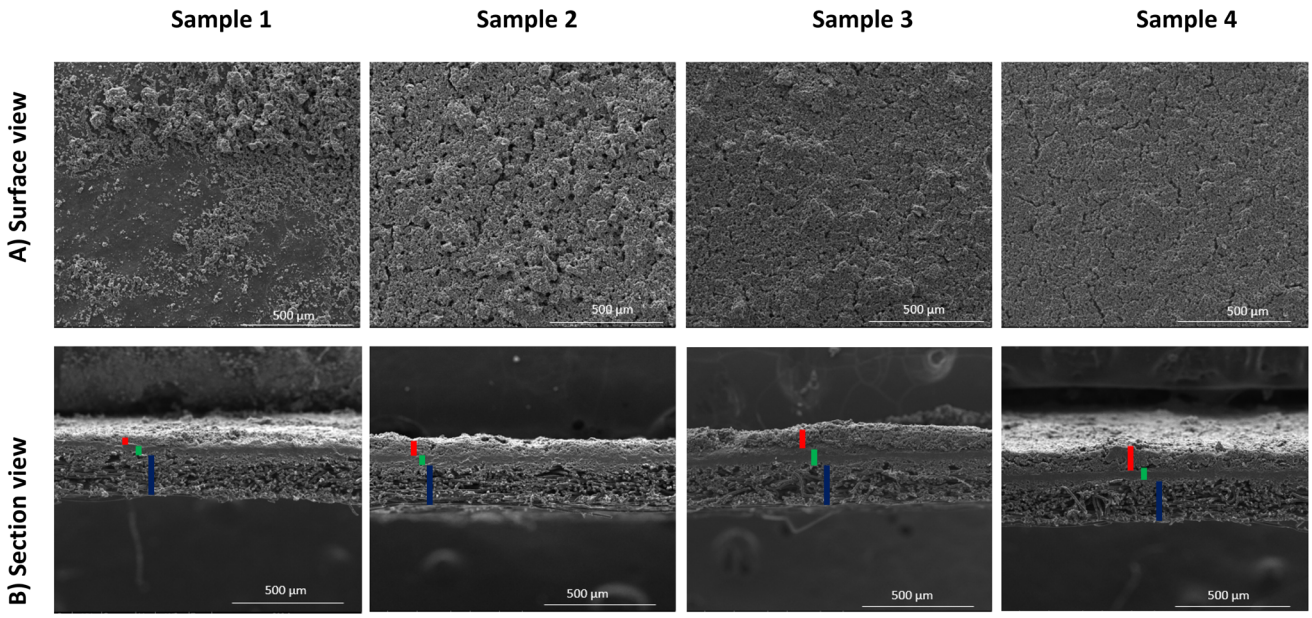

Fig. 6 (A) Surface views of the CNTs-modified GDL and samples 1, 2, 3 and 4 (B) cross-section images of the coated CNTs-modified GDL, and samples 1, 2, 3, and 4, where the red line for the coated layer, the green line for the GDL nano-porous layer (NPL) and the blue line for the GDL micro-porous layer (MPL).

4.1.4. Electrochemical performances

4.1.4.1. Doped graphene modified glassy carbon electrode. It is well known that Fe–N–C catalysts can catalyze oxygen reduction and Fe–N–C electrocatalysts have been considered as the most promising low-cost candidates to replace Pt in fuel cells. This type of catalyst has been studied deeply in acidic and alkaline environments but only one study in neutral media was reported.[19] The electrocatalytic activity of our iron (2%)/nitrogen-doped graphene toward oxygen was evaluated by cyclic voltammetry (CV) in a physiological buffer. Fig. 7 shows cyclic voltammograms (CVs) recorded under azote and oxygen-saturated solutions. Under oxygen conditions, the CVs exhibited a clear sigmoidal catalytic wave that corresponds to a typical behavior of an electro-catalytic reduction of oxygen starting at 0.18 V *vs.* SCE, and reaching a maximum current density value of 2.7 mA cm^{-2}. However, in the absence of oxygen (nitrogen purged solution), no catalytic current was observed and the CV only reflects the catalyst featureless capacitive current. These

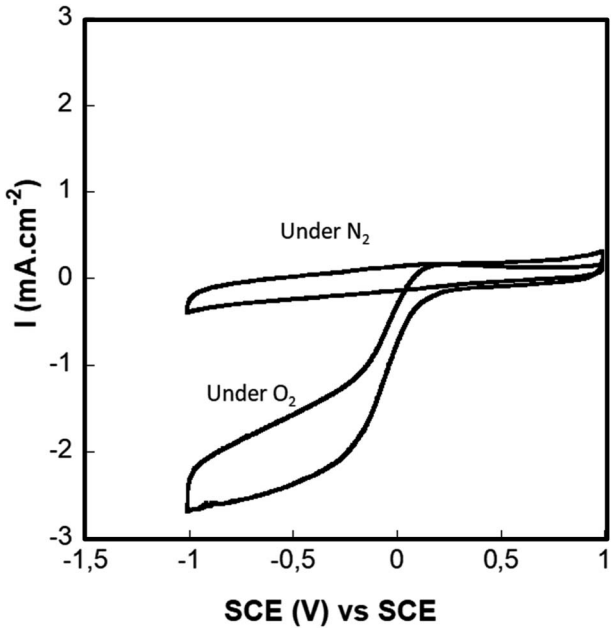

Fig. 7 Cyclovoltammetry of the D. Gr under air, nitrogen and oxygen, in a PBS pH = 7.4 at a scan rate of 10 mV s^{-1} and RDE speed of 500 rpm.

results indicate the catalyst's nitrogen-purged capacity to catalyze ORR under physiological media which is in agreement with the reported results by Ketpang *et al.*[19] demonstrating the capacity of nitrogen/Iron doped carbon catalyst to catalyze the ORR in neutral PBS media at physiological pH.

4.1.4.2. Iron/nitrogen doped graphene (D. Gr) based flexible cathode. The electrochemical performances of the D. Gr based flexible cathodes were evaluated by chronoamperometry measurements at a potential equal to 0.1 V *vs.* SCE in physiological buffer. These measurements were realized for the cathodes with different ratios under air and saturated oxygen conditions (Fig. 8). We choose to work at 0.1 V *vs.* SCE because generally when the biocathode is associated with an anode to build fuel cells, the anode potential is often equal to or less than 0 V. For all the cathodes, we observe that the buffer solution's oxygen saturation induces an increase in the reduction current.[22] This is in agreement with the results obtained and discussed above concerning the D. Gr based glassy carbon ability to electro catalyze the oxygen reduction under physiological pH. The highest current densities of 66 μA cm^{-2} under air and 84 μA cm^{-2} under oxygen were obtained with sample 2 (see Fig. S2† and Table 4). These results are in line with the coated layers characterization discussed in the previous part. For samples 1, 3, and 4 poor adhesions due either to the low binder proportion or the crackle's presence was noticed. This one causes the coated layer release in the electrolyte solution while doing the electrochemical tests. Thus, inducing poor stability over time and a low electrochemical activity compared to sample 2 (see Table 4). However, the differences between the values of the obtained current under air and under oxygen are not very significant. This low difference could be explained by

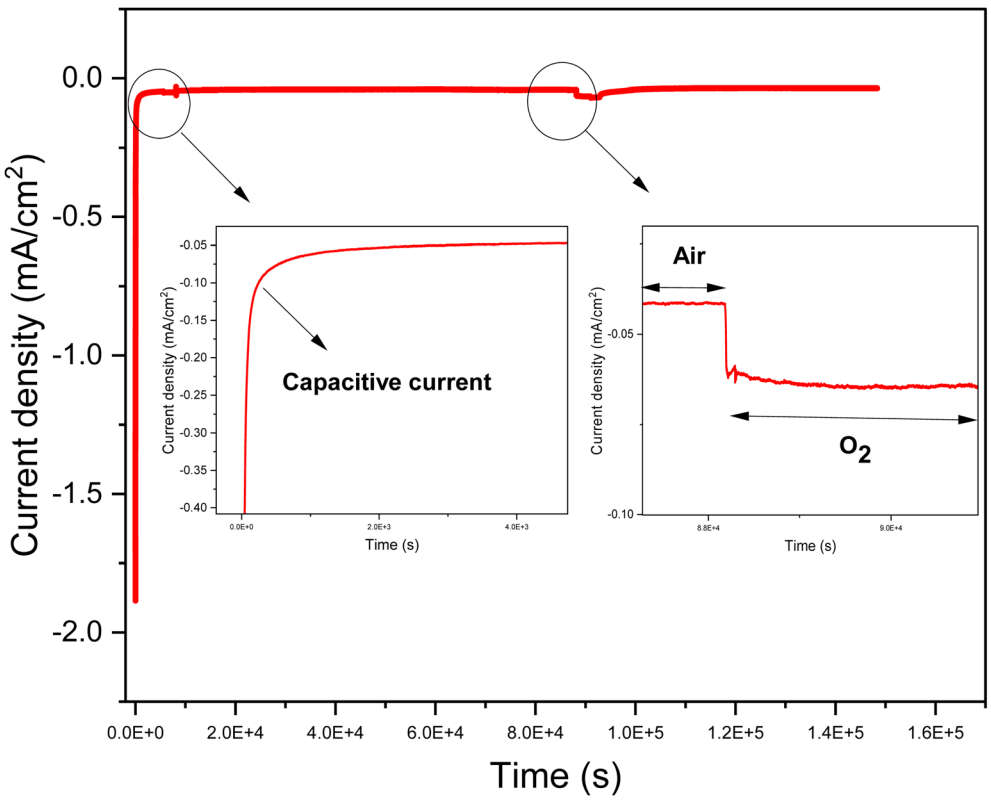

Fig. 8 An example of chronoamperometry of sample 3 at 100 mV *vs.* SCE in 100 mL of a solution containing phosphate buffer (0.01 mol L^{-1}), pH = 7.4, and at ambient temperature (20 ± 3 °C).

Table 4 Summary table of the current densities delivered under air and saturated oxygen for the different samples

	Current under air ($\mu A\ cm^{-2}$)	Current under oxygen ($\mu A\ cm^{-2}$)
Sample 1	14	31
Sample 2	66	84
Sample 3	39	75
Sample 4	41	68

the fact that the catalytic current is not only limited by the oxygen concentration and its diffusion, but other parameters may intervene such as protons concentration and the biocathode permeability to oxygen. In the case of biocathode-based on no doped graphene, the current density is almost zero even under oxygen saturation conditions (Fig. S1, ESI†). This indicates that iron-nitrogen catalytic sites present the electrocatalytic activity origin toward oxygen reduction of the prepared flexible biocathodes. As shown in Fig. 8, these flexible electrodes exhibit a relatively high capacitive current. This result is highly expected since graphene has sparked a lot of interest in supercapacitor research due to its two-dimensional structure, which gives it unique qualities like greater electrical conductivity and mechanical properties, as well as a larger surface area compared to carbon nanotubes (CNTs).[47,48]

To summarize, the results obtained by the CVs and the chronoamperometry tests demonstrate the D. Gr ability to electro-catalyze the ORR at a physiological pH, which is, from our point of view, an important result demonstrating the potential of the iron-nitrogen doped graphene (D. Gr) as a catalyst in the development of implantable abiotic cathodes. For *in vivo* applications, the electrochemical performances are generally presented per volume either per surface since for implantable devices, and from a medical point of view, the volume expression is more suitable. Furthermore, and taking into account our cathode's volume, the delivered catalytic current density values are 3 mA cm^{-3} under air and 4 mA cm^{-3} under oxygen. These performances are close to our previous results on laccase-based MWCNTs cathodes for implantable BFCs.[22]

4.1.4.3. The cathode stability study. Generally, and as a function of the supplied implanted device, the implantable electrical generators (such as lithium-ion based batteries) lifetime varies from 4 years to 7 years which is medically accepted. Thus, implantable abiotic BFCs must exhibit long-term stability at least closest to implantable lithium-ion batteries. For this reason, the main implantable abiotic cathode's challenge is their capacity of preserving their electrocatalytic activity toward oxygen reduction during a long period. In the case of Fe–N–C catalysts, many parameters affect the long-term stability of the catalysts such as the resistance of carbon materials to corrosion and the presence or not of hydrogen peroxide, a possible product of oxygen reduction reaction, which can be a source of catalyst poising. In order to investigate the stability issue of our flexible biocathodes, long-term stability has been evaluated by

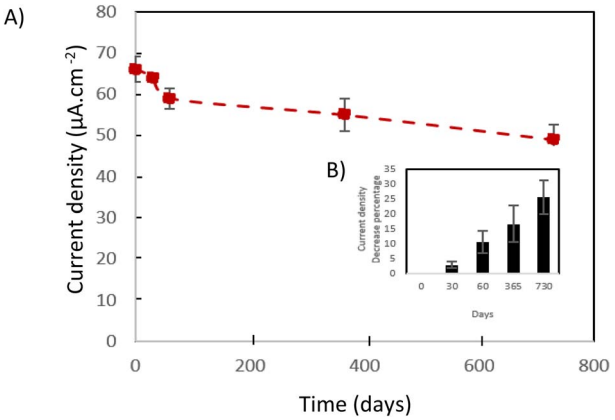

Fig. 9 (A) current density in the function of the time. (B) Current density decrease percentage in the function of the time.

periodic chronoamperometric measurement at 0.1 V *vs.* SCE in PBS buffer (pH 7.4). Fig. 10A summarizes the evolution of current density values as a function of time. We can observe the presence of two zones: the first one corresponds to an important decrease of the current density value during the first 2 months almost 10% of its initial value. The second zone starts after the second month. For this one, a slower current density decrease over time is noticed. We have only a 15% loss during the 22 following months. Overall, after storage in PBS buffers for 2 years, our flexible biocathodes have a high capacity to preserve their electrocatalytic activity. The recorded loss is in the same order as what we can observe in the case of other electrochemical generators such as batteries and fuel cells. We can attribute this long-term stability to (i) the high resistance of graphene to corrosion, (ii) the low load of produced H_2O_2 under physiological pH (iii) the presence of chitosan binder that enhances significantly the mechanical stability of the biocathode. These results are in agreement with Ketpang *et al.*[19] who studied the nitrogen/iron-doped carbon catalyst (Fe–N–C) stability but only for 3 hours. They demonstrate that the current decrease of Pt/C catalyst was faster than the one of the Fe–N–C catalysts. Thus, they deduce that the Fe–N–C catalyst was durable to operate under neutral media showing a promising ORR electroactivity to replace the expensive Pt/C catalyst. To the best of our knowledge, these are the first results demonstrating the stability of an abiotic cathode under physiological pH during a long period. This long-term stability of our flexible biocathode made them a promising choice for implantable applications (Fig. 9).

4.1.5. *In vitro* biocompatibility test. The implantation of any device can be considered only if its biocompatibility is demonstrated through *in vitro* and *in vivo* investigations. Biocompatibility of an implantable device is defined by its ability to work properly once implanted in the body without causing risks of injury (due for example to an unsuitable geometry, toxicity, or rejection by the immune system). The main goal of this section is to evaluate the ability to implant the printed biocathodes without causing rejection reactions or risk to the animal. Thus, we studied the different flexible

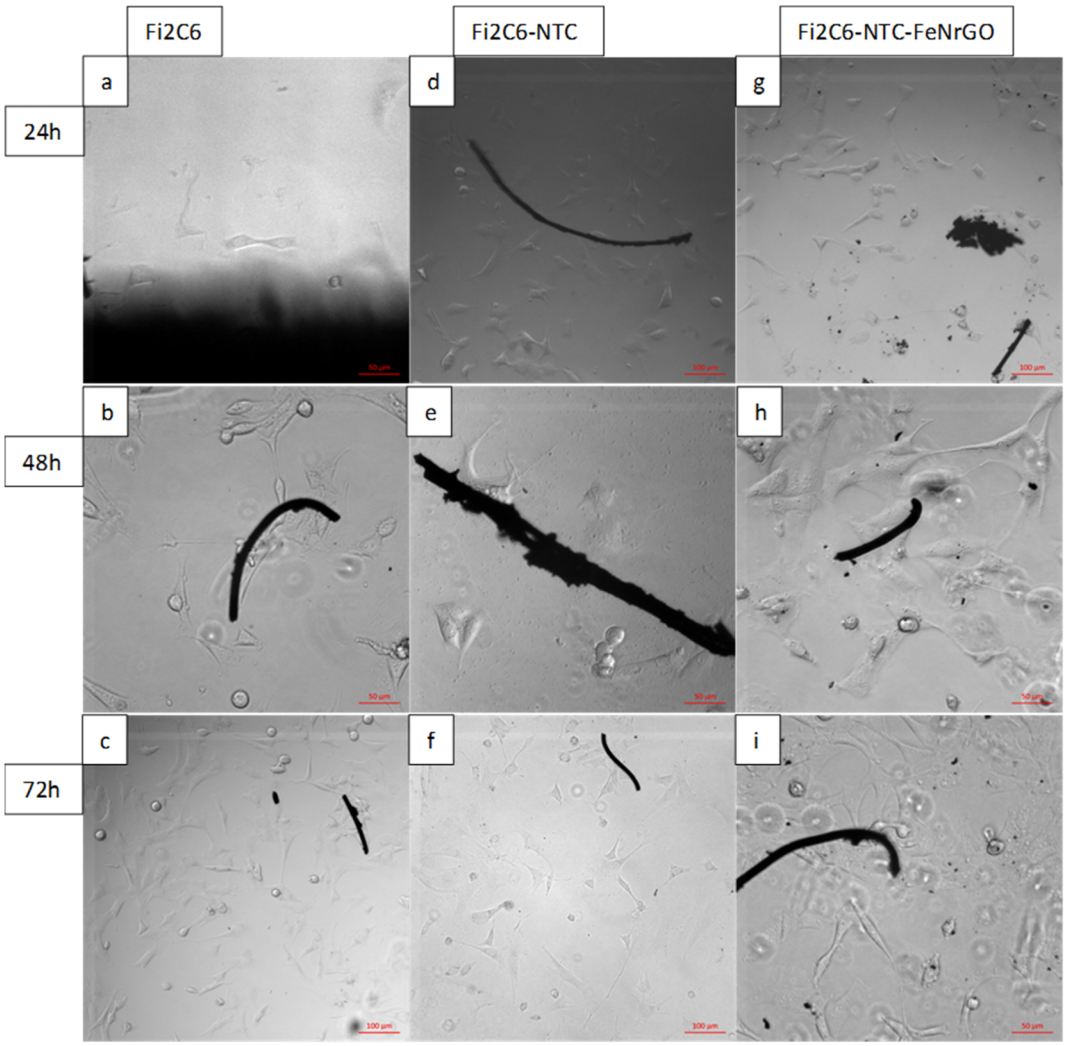

Fig. 10 Pictures of 3T3-NIH adhered (24 hours) and grown (24, 48, and 72 hours) in presence of the GDL, GDL-CNTs, and GDL-CNTs-D. Gr.

biocathodes compound (GDL, GDL-CNTs-based coating, and the GDL with the CNTs and the iron nitrogen-doped graphene-based coating) cytotoxicity. Fig. 10a–i show cell culture of fibroblasts (3T3-NIH) in presence of the GDL, GDL-CNTs, and GDL-CNTs-D. Gr after 24, 48, and 72 hours. 24 hours after adding 1×10^4 3T3-NIH cells, the cell's morphologies were analyzed by photonic microscopy. Fig. 10a–c show adhered and fusiform 3T3 cells in contact with the gas diffusion layer material. Besides, these figures also show the presence of cells in ring form. Fig. 10 shows 2 cells in a specific proliferation step known as metaphase. Regarding those results, 3T3-NIH cells can adhere and proliferate in presence of the commercial teflonated gas diffusion layer (GDL), but the presence of cells in ring configuration highlights difficulties of the cell adhesion receptors to perform their task. In the case of GDL sprayed with CNTs (GDL-CNTs), Fig. 10d–f show similar behavior results compared to the GDL material but lower ring cells. Fig. 10f shows cells close to the confluence. Compared with the previous results, the presence of the sprayed CNTs layer provides a better cell adhesion compared to the commercial teflonated gas diffusion layer material. In the case of the flexible cathodes (GDL-CNTs-D. Gr), cells seem to adhere well to the surface of the material and no cells in ring configuration were observed (Fig. 10g–i). Thus, the D. Gr addition could improve cell adhesion in this situation. Fig. 10i shows cells at the confluence, revealing that D. Gr addition should impact cell proliferation. However, Fig. 10g–i show that D. Gr particles can cross the cell membrane, which could influence the cell culture for a longer period.

The cell-material interaction was studied and compared for the different samples: GDL, GDL-CNTs, and GDL-CNTs-D. Gr. Fig. 11 demonstrates the 3T3-NIH growth for these samples' groups. The number of initially adhered 3T3-NIH is similar in all three groups of samples and quite lower compared to control. Two days after seeding, the number of 3T3-NIH in presence of GDL-CNTs-D. Gr was higher than GDL-CNTs, which was higher than GDL, and all samples show cell density lower than control. This difference showed an increasing tendency in the following days of cultivation. On the 3rd day, the cell numbers were significantly higher on GDL-CNTs-D. Gr and

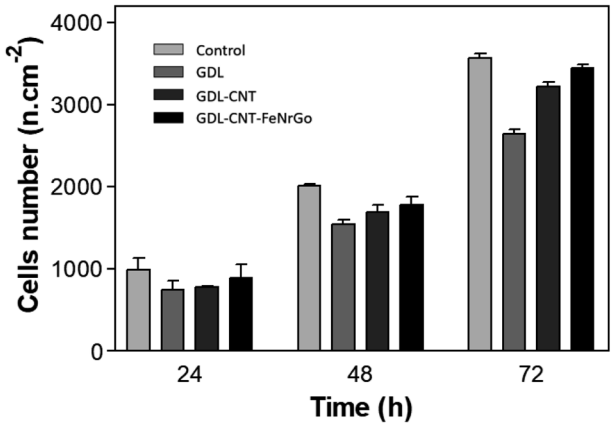

Fig. 11 Cells density in presence of materials GDL, GDL-CNTs and GDL-CNTs-D. Gr compared to the control, after 24 h, 48 h, and 72 h.

GDL-CNTs samples, especially those with graphene nanoparticles that demonstrate similar results to the control.

The lower proliferation activity of 3T3-NIH could be explained by the surface roughness and morphology of the substrate. The commercial GDL was treated with PTFE giving hydrophobic properties. Thus, hydrophobicity could decrease cell adhesion and their proliferation. In this regard, adding carbon nanotubes and then iron/nitrogen-doped graphene should decrease the impact of PTFE allowing better cell adhesion and proliferation. According to the obtained results shown in Fig. 10 and 11, it is clear that the addition of CNTs and the D. Gr affects the 3T3-NIH adhesion and proliferation. Fig. 10 shows that for the commercial GDL the cell adhesion was impacted, and Fig. 11 shows the lowest cell proliferation result for this sample, then, adding carbon nanotubes reduce the ring cell number and increase the cell adhesion, which affects the cell proliferation. The highest cell number is observed with the GDL-CNTs-D. Gr. This one gives a cell proliferation close to the one observed with the control.

From these preliminary investigations, we can assume that our flexible biocathodes don't exhibit any risk of cytotoxicity, but it is important to strengthen their mechanical solidity to prevent the release of some carbon particles that can affect negatively living cells.

5. Conclusion

In the present work, we first optimized the fabrication of flexible abiotic cathodes for implantable glucose/oxygen biofuel cells using a doctor blade coating process. According to the coated layer characterization and the electrochemical tests, a maximum current density of 66 μA cm^{-2} was obtained with doped graphene: graphene: chitosan ratio equal to 18 : 10 : 1. This ratio presented the best electrochemical performances thanks to its porosity, and good adhesion to the CNTs modified carbon substrate. The cathode stability *in vitro* was evaluated for up to 2 years, showing a faradaic current loss of only 25%. To the best of our knowledge, our results are the first demonstration of the abiotic catalyst capacity to operate under physiological pH for a long period. The cytotoxicity of the biocathode components was evaluated by cells culture experiments and results show high tolerance of living cells on the biocathode surface. This work demonstrates that this abiotic catalyst can be a promising alternative for the development of implantable glucose BFCs.

Author contributions

The manuscript was written through contributions of all authors. All authors have given approval to the final version of the manuscript.

Conflicts of interest

The authors declare that they have no known competing financial interests or personal relationships that could have appeared to influence the work reported in this paper.

Acknowledgements

This work was supported by the national research agency, France (Implantable Abiotic Biofuel Cell – IMaBiC, ANR-16-CE19-0007) France, the "Laboratoire d'Excellence" Tec21 France, Région Auvergne Rhones Alpes SCUSI program 2018 (no. 187370) and Pack Amb Int'l 2019 (no. Pack Amb Int'l 2019).

References

1 D. Zhou and E. Greenbaum, *Implantable Neural Prostheses 2: Techniques and Engineering Approaches*, Springer Science & Business Media, 2010.
2 R. Magjarević and B. Ferek-Petrić, Implantable Cardiac Pacemakers – 50 Years from the First Implantation, *Slov. Med. J.*, 2010, **79**(1), https://vestnik.szd.si/index.php/ZdravVest/article/view/224.
3 W. M. Chardack, A. A. Gage, A. J. Federico, G. Schimert and W. Greatbatch, Five years' clinical experience with an implantable pacemaker: An appraisal, *Surgery*, 1965, **58**(5), 915–922, DOI: 10.5555/uri:pii:003960606590125X.
4 F. A. Arabía, Cardiac replacement: total artificial heart, *Ann. Cardiothorac. Surg.*, 2020, **9**(2), 68, DOI: 10.21037/acs.2020.02.05.
5 R. A. Bullen, T. C. Arnot, J. B. Lakeman and F. C. Walsh, Biofuel cells and their development, *Biosens. Bioelectron.*, 2006, **21**(11), 2015–2045, DOI: 10.1016/j.bios.2006.01.030.
6 J.-P. Alcaraz, *et al.*, La biopile enzymatique à glucose/oxygène – Quelques nuances de Grays…, *Med. Sci.*, 2016, **32**(8–9), 771, DOI: 10.1051/medsci/20163208027.
7 A. Zebda, *et al.*, Single Glucose Biofuel Cells Implanted in Rats Power Electronic Devices, *Sci. Rep.*, 2013, **3**(1), 1–5, DOI: 10.1038/srep01516.
8 S. Kerzenmacher, *Abiotically catalyzed glucose fuel cells for powering energy-autonomous medical implants*, Albert-Ludwigs of Fribourg-in-Brisgau university, 2010.
9 M. Lefèvre, E. Proietti, F. Jaouen and J.-P. Dodelet, Iron-Based Catalysts with Improved Oxygen Reduction Activity

in Polymer Electrolyte Fuel Cells, *Science*, 2009, **324**(5923), 71–74, DOI: 10.1126/science.1170051.

10 X. Wang, *et al.*, N-Doping of Graphene Through Electrothermal Reactions with Ammonia, *Science*, 2009, **324**(5928), 768–771.

11 T. Cui, *et al.*, Effect of feed rate on the production of nitrogen-doped graphene from liquid acetonitrile, *Carbon*, 2012, **50**(10), 3659–3665, DOI: 10.1016/j.carbon.2012.03.038.

12 S. Bose, T. Kuila, Md. E. Uddin, N. H. Kim, A. K. T. Lau and J. H. Lee, In-situ synthesis and characterization of electrically conductive polypyrrole/graphene nanocomposites, *Polymer*, 2010, **51**(25), 5921–5928, DOI: 10.1016/j.polymer.2010.10.014.

13 K. Yuan, *et al.*, Nitrogen-doped porous carbon/graphene nanosheets derived from two-dimensional conjugated microporous polymer sandwiches with promising capacitive performance, *Mater. Chem. Front.*, 2017, **1**(2), 278–285, DOI: 10.1039/C6QM00012F.

14 H. Wang, R. Côté, G. Faubert, D. Guay and J. P. Dodelet, Effect of the Pre-Treatment of Carbon Black Supports on the Activity of Fe-Based Electrocatalysts for the Reduction of Oxygen, *J. Phys. Chem. B*, 1999, **103**(12), 2042–2049, DOI: 10.1021/jp9821735.

15 F. Jaouen, S. Marcotte, J.-P. Dodelet and G. Lindbergh, Oxygen Reduction Catalysts for Polymer Electrolyte Fuel Cells from the Pyrolysis of Iron Acetate Adsorbed on Various Carbon Supports, *J. Phys. Chem. B*, 2003, **107**(6), 1376–1386, DOI: 10.1021/jp021634q.

16 S. Stankovich, *et al.*, Graphene-based composite materials, *Nature*, 2006, **442**(7100), 282–286, DOI: 10.1038/nature04969.

17 A. Karimi, A. Othman, A. Uzunoglu, L. Stanciu and S. Andreescu, Graphene based enzymatic bioelectrodes and biofuel cells, *Nanoscale*, 2015, **7**(16), 6909–6923, DOI: 10.1039/C4NR07586B.

18 K. Wang, *et al.*, A Lactate/Oxygen Biofuel Cell: The Coupled Lactate Oxidase Anode and PGM-Free Fe–N–C Cathode, *ACS Appl. Mater. Interfaces*, 2019, **11**(45), 42744–42750, DOI: 10.1021/acsami.9b14486.

19 K. Ketpang, A. Boonkitkoson, N. Pitipuech, C. Poompipatpong, J. Sanetuntikul and S. Shanmugam, Highly Active and Durable Transition Metal-Coordinated Nitrogen Doped Carbon Electrocatalyst for Oxygen Reduction Reaction in Neutral Media, *E3S Web Conf.*, 2020, **141**, 01005, DOI: 10.1051/e3sconf/202014101005.

20 C.-H. Su, C.-L. Sun, S.-Y. Peng, J.-J. Wu, Y.-H. Huang and Y.-C. Liao, High performance non-enzymatic graphene-based glucose fuel cell operated under moderate temperatures and a neutral solution, *J. Taiwan Inst. Chem. Eng.*, 2019, **95**, 48–54, DOI: 10.1016/j.jtice.2018.09.034.

21 S. El Ichi-Ribault, *et al.*, Remote wireless control of an enzymatic biofuel cell implanted in a rabbit for 2 months, *Electrochim. Acta*, 2018, **269**, 360–366, DOI: 10.1016/j.electacta.2018.02.156.

22 B. Reuillard, *et al.*, High power enzymatic biofuel cell based on naphthoquinone-mediated oxidation of glucose by glucose oxidase in a carbon nanotube 3D matrix, *Phys. Chem. Chem. Phys.*, 2013, **15**(14), 4892–4896, DOI: 10.1039/c3cp50767j.

23 T. Miyake, S. Yoshino, T. Yamada, K. Hata and M. Nishizawa, Self-Regulating Enzyme – Nanotube Ensemble Films and Their Application as Flexible Electrodes for Biofuel Cells, *J. Am. Chem. Soc.*, 2011, **133**(13), 5129–5134, DOI: 10.1021/ja111517e.

24 L. Zhang, M. Zhou, D. Wen, L. Bai, B. Lou and S. Dong, Small-size biofuel cell on paper, *Biosens. Bioelectron.*, 2012, **35**(1), 155–159, DOI: 10.1016/j.bios.2012.02.035.

25 B. Y. C. Wan and A. C. C. Tseung, Some studies related to electricity generation from biological fuel cells and galvanic cells, *Med. Biol. Eng.*, 1974, **12**(1), 14–28, DOI: 10.1007/BF02629831.

26 I. Shitanda, S. Nohara, Y. Hoshi, M. Itagaki and S. Tsujimura, A screen-printed circular-type paper-based glucose/O_2 biofuel cell, *J. Power Sources*, 2017, **360**, 516–519.

27 I. Shitanda, S. Kato, S. Tsujimura, Y. Hoshi and M. Itagaki, Screen-printed, Paper-based, Array-type, Origami Biofuel Cell, *Chem. Lett.*, 2017, **46**(5), 726–728, DOI: 10.1246/cl.170047.

28 I. Shitanda, S. Kato, Y. Hoshi, M. Itagaki and S. Tsujimura, Flexible and high-performance paper-based biofuel cells using printed porous carbon electrodes, *Chem. Commun.*, 2013, **49**(94), 11110, DOI: 10.1039/c3cc46644b.

29 A. Ben Tahar, *et al.*, Carbon nanotube-based flexible biocathode for enzymatic biofuel cells by spray coating, *J. Power Sources*, 2018, **408**, 1–6, DOI: 10.1016/j.jpowsour.2018.10.059.

30 C. Liu, S. Alwarappan, Z. Chen, X. Kong and C.-Z. Li, Membraneless enzymatic biofuel cells based on graphene nanosheets, *Biosens. Bioelectron.*, 2010, **25**(7), 1829–1833, DOI: 10.1016/j.bios.2009.12.012.

31 S. Lanceros-Méndez and C. M. Costa, *Printed Batteries: Materials, Technologies, and Applications*, John Wiley & Sons, 2018.

32 A. Berni, M. Mennig and H. Schmidt, Doctor Blade, in *Sol-Gel Technologies for Glass Producers and Users*, ed. M. A. Aegerter and M. Mennig, Springer US, Boston, MA, 2004, pp. 89–92, DOI: 10.1007/978-0-387-88953-5_10.

33 J. R. Anusha, *et al.*, Simple fabrication of ZnO/Pt/chitosan electrode for enzymatic glucose biosensor, *Sens. Actuators, B*, 2014, **202**, 827–833, DOI: 10.1016/j.snb.2014.06.024.

34 W. H. Mullen, *Enzyme electrodes and improvements in the manufacture thereof*, *US pat.* 5160418A, 1992.

35 S. Kerzenmacher, R. Sumbharaju, J. Ducree, R. Zengerle and F. von Stetten, A Surface Mountable Glucose Fuel Cell for Medical Implants, in *Transducers 2007 – 2007 International Solid-State Sensors, Actuators and Microsystems Conference*, Lyon, France, 2007, pp. 125–128, DOI: 10.1109/SENSOR.2007.4300087.

36 S. Dinescu, *et al.*, *In vitro* cytocompatibility evaluation of chitosan/graphene oxide 3D scaffold composites designed for bone tissue engineering, *Biomed. Mater. Eng.*, 2014, **24**(6), 2249–2256, DOI: 10.3233/BME-141037.

37 L. L. Fernandes, C. X. Resende, D. S. Tavares, G. A. Soares, L. O. Castro and J. M. Granjeiro, Cytocompatibility of

chitosan and collagen-chitosan scaffolds for tissue engineering, *Polímeros*, 2011, **21**, 1–6.

38 M. Wojtoniszak, *et al.*, Synthesis, dispersion, and cytocompatibility of graphene oxide and reduced graphene oxide, *Colloids Surf., B*, 2012, **89**, 79–85, DOI: **10.1016/j.colsurfb.2011.08.026**.

39 Y. Wu, *et al.*, Reduction of graphene oxide alters its cytocompatibility towards primary and immortalized macrophages, *Nanoscale*, 2018, **10**(30), 14637–14650, DOI: **10.1039/C8NR02798F**.

40 P. K. Avti, E. D. Caparelli and B. Sitharaman, Cytotoxicity, cytocompatibility, cell-labeling efficiency, and *in vitro* cellular magnetic resonance imaging of gadolinium-catalyzed single-walled carbon nanotubes, *J. Biomed. Mater. Res., Part A*, 2013, **101**(12), 3171, DOI: **10.1002/jbm.a.34643**.

41 S. J. Bryant, C. R. Nuttelman and K. S. Anseth, Cytocompatibility of UV and visible light photoinitiating systems on cultured NIH/3T3 fibroblasts *in vitro*, *J. Biomater. Sci., Polym. Ed.*, 2000, **11**(5), 439–457, DOI: **10.1163/156856200743805**.

42 P. Ming, *et al.*, Corrosion behavior and cytocompatibility of a Co–Cr and two Ni–Cr dental alloys before and after the pretreatment with a biological saline solution, *RSC Adv.*, 2017, 7(10), 5843–5852, DOI: **10.1039/C6RA26727K**.

43 J. Yan, T. Wu, Z. Ding and X. Li, Preparation and characterization of carbon nanotubes/chitosan composite foam with enhanced elastic property, *Carbohydr. Polym.*, 2016, **136**, 1288–1296, DOI: **10.1016/j.carbpol.2015.10.049**.

44 Z. Wang, *et al.*, Modification of chitosan with monomethyl fumaric acid in an ionic liquid solution, *Carbohydr. Polym.*, 2015, **117**, 973–979, DOI: **10.1016/j.carbpol.2014.10.021**.

45 C. He, J. J. Zhang and K. Shen, Nitrogen-self-doped graphene-based non-precious metal catalyst with superior performance to Pt/C catalyst toward oxygen reduction reaction, *J. Mater. Chem. A*, 2014, **2**(9), 3231, DOI: **10.1039/c3ta14070a**.

46 A. Laaroussi, *Fabrication de biocathodes flexibles pour biopiles enzymatiques implantables par procédés d'impression*, PhD thesis, Université Grenoble Alpes, 2016.

47 M. H. Ervin, *Carbon Nanotube and Graphene-Based Supercapacitors: Rationale, Status, and Prospects*, Defense Technical Information Center, Fort Belvoir, VA, 2010, DOI: **10.21236/ADA528738**.

48 K. A. Sammed, *et al.*, Reduced holey graphene oxide film and carbon nanotubes sandwich structure as a binder-free electrode material for supercapcitor, *Sci. Rep.*, 2020, **10**(1), 2315, DOI: **10.1038/s41598-020-58162-9**.